Quantitative Characterization of Pore Corrugation in Ordered Mesoporous Materials Using Image Analysis of Electron Tomograms

Cedric J. Gommes,*[,†,‡] Heiner Friedrich,[†] Mariska Wolters,[†] Petra E. de Jongh,[†] and Krijn P. de Jong*[,†]

Department of Chemistry, Inorganic Chemistry and Catalysis, Utrecht University, Sorbonnelaan 16, 3584 Utrecht, The Netherlands, and Department of Chemical Engineering, University of Liège, Allée du 6 août 3, 4000 Liège, Belgium

Received November 13, 2008. Revised Manuscript Received January 20, 2009

Electron tomography and image analysis are combined to characterize ordered mesoporous silica SBA-15. The morphology of the mesopores with average diameter 6 nm is analyzed in terms of cylinders having variable radii and centers that are statistically centered on the points of a distorted hexagonal lattice. The variations in the mesopore centers and radii add up and result in pore wall corrugation with amplitude of 1.6 nm. The correlation length of the corrugation along the pore axis was found to be 4−5 nm. The amplitude of the corrugation compared well with the 1.9 nm thick microporous corona obtained from X-ray diffraction (XRD). In general, the present approach provides a detailed microscopic 3D model of nanostructured materials that complements macroscopic measurements such as physisorption and XRD.

1. Introduction

Controlling the morphology of a material is key in tuning its properties to specific applications. This is one of the major challenges for nanostructured materials, to obtain the desired optical,[1] electrical,[2] magnetic,[3] and catalytic[4] properties, which may depend critically on the size and shape of the constituent phases they are composed of.[5] For that reason, ordered mesoporous materials (OMM) synthesized by liquid crystal templating have attracted much attention since their discovery in 1992.[6] These materials enable the precise tuning of the pore morphology through the control of the self-organizing properties of the polymer templates.[7]

SBA-15 is one of the OMM that has been the most extensively studied.[8,9] It is mesoporous silica, the structure of which is approximated by a 2D hexagonal array of uniformly sized cylindrical pores with a diameter ranging from 5 to 30 nm, depending on the synthesis procedure. The use of SBA-15 covers a broad range of domains, including the development of catalysts,[10] adsorbent materials,[11] and nanoparticles,[12] but also research aiming at understanding the effect of confinement on phase diagrams[13] or the process of capillary condensation and evaporation in mesopores.[14,15] In all cases, a thorough understanding of the material morphology is needed.

Several experimental techniques can be used for the morphological characterization of mesoporous materials, such as physisorption,[16−20] X-ray diffraction (XRD),[21,22] mercury intrusion porosimetry,[23] and microscopy.[24−29] Bulk techniques like physisorption or XRD provide an average description of the material in terms of specific surface area, pore size, wall thickness, unless specific morphological

---

* Corresponding author. E-mail: cedric.gommes@ulg.ac.be (C.J.G.); k.p.dejong@uu.nl (K.P.d.J.).

[†] Utrecht University.

[‡] University of Liège.

(1) Yang, P.; Wirnsberger, G.; Huang, H.; C.; Cordero, S. R.; McGehee, M. D.; Scott, B.; Deng, T.; Whitesides, G. M.; Chmelka, B. F.; Buratto, S. K.; Stucky, G. D. *Science* **2000**, *287*, 465.

(2) Ebbesen, T. W.; Lezec, H. J.; Hiura, H.; Bennett, J. W.; Ghaemi, H. F.; Thio, T. *Nature* **1996**, *382*, 54.

(3) Majetich, S. A.; Jin, Y. *Science* **1999**, *284*, 470.

(4) Bezemer, G. L.; Bitter, J. H.; Kuipers, H. P.; C, E.; Oosterbeek, H.; Holewijn, J. H.; Xu, X.; Kaptein, F.; van Dillen, A. J.; de Jong, K. P. *J. Am. Chem. Soc.* **2006**, *128*, 3956.

(5) Roduner, E. *Chem. Soc. Rev.* **2006**, *35*, 583.

(6) Beck, J. S.; Vartuli, J. C.; Roth, W. J.; Leonowicz, M. E.; Kresge, C. T.; Schmidtt, K. D.; Chu, C. T.-W.; Sheppard, E. W.; McCullen, S. B.; Higgins, J. B.; Schlenkert, J. L. *J. Am. Chem. Soc.* **1992**, *114*, 10834.

(7) Förster, S.; Plantenberg, T. *Angew. Chem., Int. Ed.* **2002**, *41*, 688.

(8) Zhao, D.; Feng, J.; Huo, Q.; Melosh, N.; Fredrickson, G. H.; Chmelka, B. F.; Stucky, G. D. *Science* **1998**, *279*, 548.

(9) Schüth, F.; Schmidt, W. *Adv. Mater.* **2002**, *14*, 629.

(10) Sietsma, J. R. A.; Meeldijk, J. D.; den Breejen, J.; Versluijs-Helder, M.; van Dillen, A. J.; de Jongh, P. E.; de Jong, K. P. *Angew. Chem., Int. Ed.* **2007**, *46*, 4547.

(11) Hoang, V.-T.; Huang, Q.; Eic, M.; Do, T.-O.; Kaliaguine, S. *Langmuir* **2005**, *21*, 2051.

(12) Gao, F.; Lu, Q.; Liu, X.; Yan, Y.; Zhao, D. *Nano Lett.* **2001**, *1*, 743.

(13) Dosseh, G.; Yongde, X.; Alba-Simionesco, C. *J. Phys. Chem. B* **2003**, *107*, 6445.

(14) Grosman, A.; Ortega, C. *Langmuir* **2005**, *21*, 10515.

(15) Morishige, K. *Adsorption* **2008**, *14*, 157.

(16) Lukens, W. W.; Schmidt-Winkel, P.; Zhao, D.; Feng, J.; Stucky, G. D. *Langmuir* **1999**, *15*, 5403.

(17) Ravikovitch, P. I.; Neimark, A. V. *J. Phys. Chem. B* **2001**, *105*, 681.

(18) Galarneau, A.; Cambon, H.; Di Renzo, F.; Fajula, F. *Langmuir* **2001**, *17*, 8328.

(19) Groen, J. C.; Peffer, L. A. A.; Perez-Ramırez, J. *Microporous Mesoporous Mater.* **2003**, *60*, 1.

(20) Gommes, C. J.; Ravikovitch, P.; Neimark, A. *J. Colloid Interface Sci.* **2007**, *314*, 415.

(21) Imperor-Clerc, M.; Davidson, P.; Davidson, A. *J. Am. Chem. Soc.* **2000**, *122*, 11925.

(22) Förster, S.; Timman, A.; Konrad, M.; Schellbach, C.; Meyer, A.; Funari, S. S.; Mulvaney, P.; Knott, R. *J. Phys Chem B* **2005**, *109*, 1347.

(23) Galarneau, A.; Lefèvre, B.; Cambon, H.; Coasne, B.; Valange, S.; Gabelica, Z.; Bellat, J.-P.; Di Renzo, F. *J. Phys. Chem. C* **2008**, *112*, 12921.

10.1021/cm803092c CCC: $40.75

models are used (for example, see ref 20). On the other hand, electron microscopy and electron tomography can provide a spatially resolved and model-free characterization of nanomaterials. In particular, the 3D structural information obtained from tomography holds great potential for quantification by image analysis.[26,28,30,31] However, sampling is problematic because the total mass of sample analyzed rarely exceeds 1×10^{-13} g. Therefore, the thorough characterization of nanostructured materials can only be achieved by combining bulk characterization with local microscopic techniques.

It is generally acknowledged that several different morphological and physical models have to be tested to analyze characterization data of different nature before a consensus progressively emerges. In the case of SBA-15 in particular, the simple cylindrical mesopore model proved soon to be insufficient. The morphology of these materials include a complementary porosity connecting laterally the main channels,[32,33] a significant microporosity,[17,18] and a marked roughness of the pore surface compatible with both XRD[21] and physisorption[34] data. The XRD data can, however, be equally well analyzed in terms of the randomness of the pore positions and sizes.[21,22] Within such models, randomness is not distinguishable from the corrugation of the pore surface[35] apparent in high resolution transmission electron micrographs.[24] Therefore, the exact interpretation of the bulk characterization data, in terms of the morphology of SBA-15, remains a challenge.

In the present paper, we combine image analysis with electron tomography (3D-TEM)[36,37] to quantitatively characterize the local morphology of SBA-15, and notably the corrugation of the mesopore walls. Image analysis is done in such a way as to enable a straightforward comparison with the morphological models used to analyze bulk characterization data.[21,34]

2. Materials and Methods

SBA-15 was prepared via a method adapted from Zhao et al.:[8] 8 g of PEG20PPG70PEG20 (PEG = poly(ethyleneglycol; PPG = poly(propyleneglycol)) triblock copolymer (Aldrich) was dissolved in 250 mL of demineralized water at 40 °C. After the solution had become clear, 48 g of 11.6 M hydrochloric acid was added, followed by the addition of 21.5 mL of tetraethoxysilane (Acros). The mixture was stirred for 20 h at 40 °C and then transferred to an oven for further reaction at 80 °C for 48 h. The solid product was collected from the suspension by filtration, washed, dried in air for 12 h at 80 °C, and calcined for 6 h at 550 °C.

Low-angle XRD of SBA-15 was measured at the Dutch-Belgian SRG beam line (BM26B) at the European Synchrotron Radiation Facility (Grenoble, France), on a 2D detector placed at 3.5 m from the sample. The scattered intensity was rotationally averaged and expressed as the intensity as a function of the scattering vector modulus $q = (4\pi/\lambda)\sin(\theta/2)$, λ being the wavelength and θ the scattering angle. The intensity scattered by the empty sample holder was subtracted from the data, and a correction was made for the detector response. Nitrogen adsorption and desorption isotherms were measured at −196 °C on a Micromeritics Tristar 3000 volumetric device.

TEM samples were prepared by crushing a small amount of the calcined material (~10−15 mg) in a mortar and subsequently depositing a portion of the obtained fine powder directly onto a Quantifoil R2/1 carbon support film. Excess material was shaken off by gently tapping the grid edge on a filter paper. The carbon support film contained an additional continuous 2−3 nm thick carbon layer to which 5 nm colloidal gold particles were applied prior to deposition of the sample material. After dry deposition of SBA-15, an additional thin carbon layer was coated on top of the particles.

Electron tomography was performed in bright-field mode using a Tecnai 20 electron microscope (FEI Company, Eindhoven). Images of three tilt-series were acquired over an angular range of ±76° at 2° increments on a Tietz 2k × 2k CCD camera (TVIPS Gmbh, Gauting) using Inspect3D software (FEI Company, Eindhoven). A movie of the tilt series is available in the Supporting Information (SI-1). The nominal magnification was 29000 × corresponding to a pixel size of 0.27 nm. A nominal defocus of −100 to −200 nm was chosen such that the entire object was imaged in underfocus throughout the tilt-series. The applied dose was estimated to less than 3000 $e^-/Å^2$ for each of the three tilt series. Such a low dose was needed because the samples were found to be beam-sensitive.

Images of the tilt-series were aligned with respect to a common origin and rotation axis using the 5 nm gold particles as fiducial markers. Finally the aligned tilt-series was binned to 0.54 nm pixel size prior to reconstruction of the three-dimensional volume. Alignment and reconstruction of the tilt series was performed in IMOD;[38] subsequent image analysis was done with Matlab. Visualizations of the qualitative 3D morphology were carried out in Amira 3.1 (TGS, Inc.) after nonlinear anisotropic diffusion filtering.[39]

It is difficult to assess the actual resolution of the reconstructions based e.g. on Crowther's criterion,[37] as this is known to lead to an underestimation. From a previous work with a similar setup in which objects of 1.5 nm across could be measured,[26] we infer that the resolution of the reconstructions in the present work is about 1.5 nm^3.

3. Results

3.1. Bulk Characterization of SBA-15. The low-angle XRD pattern of SBA-15 is displayed in Figure 1a. It shows distinct maxima, the positions of which are in agreement

---

(24) Liu, Z.; Terakasi, O.; Ohsuna, T.; Hiraga, K.; Shin, H. J.; Ryoo, R. *Chem. Phys. Chem.* **2001**, *4*, 229.
(25) Janssen, A. H.; Van Der Voort, P.; Koster, A. J.; de Jong, K. P. *Chem. Commun.* **2002**, 1632.
(26) Friedrich, H.; Sietsma, J. R. A.; de Jongh, P. E.; Verkleij, A. J.; de Jong, K. P. *J. Am. Chem. Soc.* **2007**, *129*, 10249.
(27) Han, Y.; Zhao, L.; Ying, J. Y. *Adv. Mater.* **2007**, *19*, 2454.
(28) Yuan, P.; Liu, N.; Zhao, L.; Zhou, X.; Zhou, L.; Auchterlonie, G. J.; Yao, X.; Drennan, J.; Lu, G. Q.; Zou, J.; Yu, C. *Angew. Chem., Int. Ed.* **2008**, *47*, 6670.
(29) Tüysüz, H.; Lehmann, C. W.; Bongard, H.; Tesche, B.; Schmidt, R.; Schüth, F. *J. Am. Chem. Soc.* **2008**, *130*, 11510.
(30) Gommes, C. J.; de Jong, K. P.; Pirard, J.-P.; Blacher, S. *Langmuir* **2005**, *21*, 12378.
(31) Jinnai, H.; Shinbori, Y.; Kitaoka, T.; Akutagawa, K.; Mashita, N.; Nishi, T. *Macromolecules* **2007**, *40*, 6758.
(32) Kruk, M.; Jaroniec, M.; Ko, C. H.; Ryoo, R. *Chem. Mater.* **2000**, *12*, 1961.
(33) Ryoo, R.; Ko, C. H.; Kruk, M.; Antochshuk, V.; Jaroniec, M. *J. Phys Chem. B* **2000**, *104*, 11465.
(34) Ravikovitch, P. I.; Neimark, A. V. *Langmuir* **2006**, *22*, 11171.
(35) Hofmann, T.; Wallacher, D.; Huber, P.; Birringer, R.; Knorr, K.; Schreiber, A.; Findenegg, G. H. *Phys. Rev. B* **2005**, *72*, 064122.
(36) Ziese, U.; de Jong, K. P.; Koster, A. *J. Appl. Catal., A* **2004**, *260*, 71.
(37) Weyland, M.; Midgley, P. A. *Mater. Today* **2004**, *7*, 32.
(38) Kremer, J. R.; Mastronarde, D. N.; McIntosh, J. R. *J. Struct. Biol.* **1996**, *116*, 71.
(39) Frangakis, A. J.; Hegerl, R. *J. Struct. Biol.* **2001**, *135*, 239.

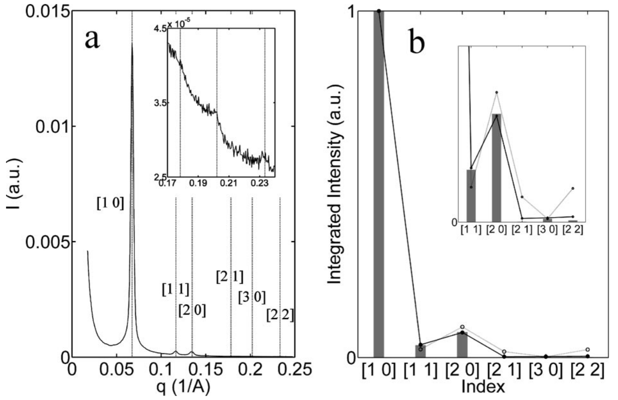

Figure 1. (a) Low-angle XRD pattern of SBA-15 with the vertical lines being the expected positions of the peaks of a 2D hexagonal structure with lattice parameter $a = 10.8$ nm; (b) integrated intensities of the peaks and their best fit with a smooth cylindrical pore model (gray line) and with the linear corona model (solid line).

with a 2D hexagonal lattice[8] with a unit cell of size $a = 10.8$ nm. The integrated intensities of the peaks, determined by a fitting with a pseudo-Voigt model are shown in Figure 1b. Following the method proposed by Impéror-Clerc et al.,[21] the relative intensities were fitted by least-squares to the smooth cylindrical pore model and to the linear corona model. The integrated peak intensities cannot be properly accounted for by smooth cylindrical pores (best fit with radius of 3.6 nm, gray line in Figure 1b), but the fitting with the linear corona is satisfactory (black line, Figure 1b); the corona is found to extend from radial distance $r = 2.7$ nm to $r = 4.6$ nm.

Nitrogen adsorption and desorption isotherms were analyzed using a *t*-plot analysis,[40] with LiChrospher S1−1000[41,20] as a nonporous reference (see the Supporting Information, SI-3). The total and microporous volumes are $V_{\mathrm{tot}} = 0.66$ cm^3/g and $V_{\mathrm{micro}} = 0.09$ cm^3/g, the difference between the two values being attributed to mesopores $V_{\mathrm{meso}} = 0.57$ cm^3/g; the mesopore surface area, is $S_{\mathrm{meso}} = 419$ m^2/g. Using the Broekhof-deBoer theories of capillary condensation[42] and evaporation[43] in cylindrical mesopores, the average mesopore diameter is estimated to be 5.6 nm from the adsorption isotherm and 6.4 nm from the desorption isotherm.

3.2. Electron Tomography. A first view on the pore structure in SBA-15 is given in Figure 2. Both, TEM image (Figure 2a) and reconstructed intensity map (Figure 2b) display the overall particle morphology and pore ordering, but reveal little information on the corrugation of the pores. A clearer picture is obtained by extrapolating the silica surface (images c and d in Figure 2). Qualitatively, the 2D hexagonal ordering is evident and pores are corrugated on the nanometer scale. A movie through the reconstruction is given in the Supporting Information (SI-2).

3.3. Image Analysis. It is worth stressing that the segmented tomograms in images c and d in Figure 2 were obtained after filtering the data. Although filtering-based segmentation can provide qualitative insight into the pore morphology, it cannot be used for a reliable quantitative characterization. A different image analysis approach is therefore used in the present paper that is based on a parametrized morphological model, the parameters of which are optimized to fit the reconstructions at best. The use of a morphological model enables to cope with the noise present in the reconstructions without having to use filters, and to estimate the morphological parameters with a better accuracy than the nominal resolution of the reconstruction.[44]

The morphological model we use consists in assuming that the sections of the mesopores in SBA-15 are disks, the radii and centers of which are variable in an a priori unknown way along the pore direction. The image analysis comprises three successive steps, namely the determination of the pore direction, the estimation of the local radii and centers of the pores sections, and the statistical analysis of radii and centers in terms of the corrugation of the pores. An examination of the sensitivity to noise and resolution of the entire image analysis is presented in the Supporting Information (SI-3).

Each reconstruction contains regions with calcined SBA-15, the carbon support film, the gold markers, and empty space surrounding the materials. For processing, the full reconstruction was cut into regions of size 128 × 128 × 128 pixels, containing only SBA-15. An example of such a 3D region is shown in Figure 3a; it is approximately 2 times larger than the region shown in images c and d in Figure 2. The present paper is based on the analysis of a total of 10 such regions, taken from the reconstruction of 3 distinct particles similar to that in Figure 2b.

3.3.1. Determination of Pore Orientation. The 128^3-sized regions are chosen to be large enough to contain a few tens of pores, and small enough for the pores to have a well-defined orientation (Figure 3a) excluding too severe bending of the pores as previously observed over larger domains.[25,45] The first step of the image analysis is to determine the average pore orientation. This is done by calculating the autocorrelation function of the gray-tone 3D images. Letting $I(\mathbf{x})$ be the intensity of the tomogram at the 3D position $\mathbf{x}$, the autocorrelation of the image is defined as[46−48]

$$C(\mathbf{r}) = \frac{\langle (I(\mathbf{x}+\mathbf{r}) - \langle I(\mathbf{x})\rangle)(I(\mathbf{x}) - \langle I(\mathbf{x})\rangle)\rangle}{\langle (I(\mathbf{x}) - \langle I(\mathbf{x})\rangle)^2\rangle} \qquad (1)$$

where $\langle\rangle$ denotes the average value, calculated on all pairs of pixels separated by the vector $\mathbf{r}$; $C(\mathbf{r})$ characterizes the global translational invariance of the gray levels in the 3D image in the direction and distance given by $\mathbf{r}$.

Figure 3b shows the areas of the autocorrelation of Figure 2a, where the correlation is larger than $C = 0.2$. The displayed areas correspond to translations that leave the gray tones almost unchanged. Elongation points to the fact that

---

(40) Gregg, S. J.; Sing, K. S. W. *Adsorption, Surface Area and Porosity*; Academic Press: London, 1982.

(41) Jaroniec, M.; Krul, M.; Olivier, J. P. *Langmuir* **1999**, *15*, 5410.

(42) Broekhoff, J. C. P.; De Boer, J. H. *J. Catal.* **1967**, *9*, 8.

(43) Broekhoff, J. C. P.; De Boer, J. H. *J. Catal.* **1968**, *10*, 368.

(44) Bobroff, N. *Rev. Sci. Instrum.* **1986**, *57*, 1152.

(45) Che, S.; Lund, K.; Tatsumi, T.; Iijima, S.; Joo, S. H.; Ryoo, R.; Terasaki, O. *Angew. Chem., Int. Ed.* **2003**, *42*, 2182.

(46) Serra, J. *Image Analysis and Mathematical Morphology*; Academic Press: London, 1984.

(47) Russ, J. C. *The Image Processing Handbook*; CRC Press: Boca Raton, FL, 2002.

(48) Press, W.; Teukolsky, S.; Vetterling, W.; Flannery B. *Numerical Recipes in C: The Art of Scientific Computing*, 2nd ed.; Academic Press: New York, 1992.

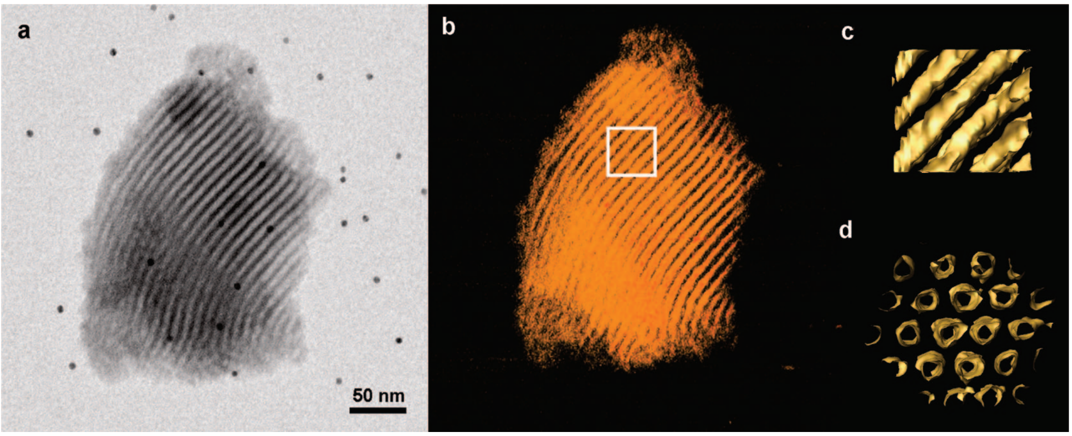

Figure 2. (a) TEM image of the tilt series, (b) reconstructed intensity map, and (c,d) extrapolated silica surface in a 64^3 pixel sized volume after applying a non linear anisotropic diffusion filter. The position of the volume displayed in (c,d) is indicated in (b).

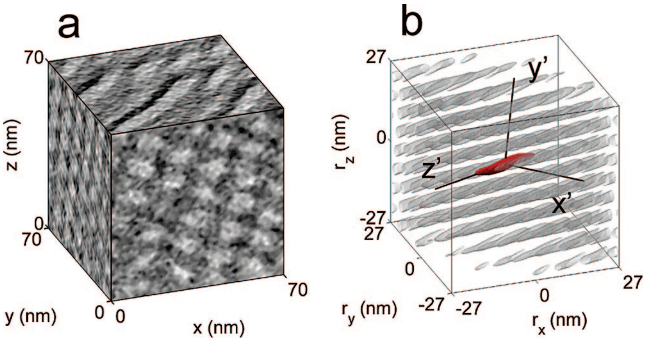

Figure 3. (a) Tomogram of SBA-15 and (b) its autocorrelation function. The central lobe of the autocorrelation function (in red) is used to determine the average pore orientation, from which the new axes x', y', and z' are determined.

the tomogram is invariant with respect to translations along the pores. Each gray area corresponds to a translation by which one mesopore is overlapped with one neighbor. A principal component analysis[48] of the central region of the autocorrelation function (red in Figure 3b) is done, from which the average orientation of the mesopores is obtained.

On the basis of the obtained pore direction, new coordinates are created with the axes z' parallel to the mesopores (Figure 3b). The new axis y' is chosen to have the smallest possible angle with the initial direction z, and x' is orthogonal to both z' and y'. Keeping track of the initial orientation z is useful in the further data analysis because the resolution of the tomograms is lower in that direction as a result of the limited maximum tilt angle during data acquisition.[49]

3.3.2. Local Determination of the Pore Center and Radius. Once the orientation of the mesopores is known, the tomograms are analyzed slice by slice, with the slices taken orthogonal to the mesopores (Figure 4a). To detect, the pore centers, a moving average filter was applied to each slice with a Gaussian kernel having a standard deviation of 5 pixels. That particular size of 5 pixels was chosen because it is close to the pore radius. The centers of the pores are given by the local maxima of the intensity in the filtered slices (Figure 4b). The resulting centerlines of this slice-by-slice search are displayed in Figure 4c; the figure indicates that all pores are tortuous.

Once the position of the center of each pore at each height z' is known, the local radius of the pore is estimated via the method shown in Figure 5. The intensity of all pixels of the z'-slice at a given distance from the center is averaged (Figure 5a), which provides an intensity profile that starts from high values in the center of the pore and decreases progressively with increasing radius (Figure 5b). The two horizontal lines in Figure 5b correspond to the average intensities of the silica and of the pores, obtained by projecting the tomogram along direction z'. In an ideal imaging setup with a vanishingly small resolution, the intensity transition between pore and silica would have occurred over a very short distance. In practice, however, because of the finite resolution of the reconstruction, the actual transition in Figure 5b spreads over a distance close to 2 nm, which compares well with the resolution of 1.5 nm estimated in section 2. Although the exact analytical form of the point-spread-function of the reconstruction is unknown, it is reasonable to assume that the transition region is centered on the actual radius of the pore. We therefore determine the local radius of the pores as the distance from the center at which the intensity is exactly intermediate between the intensities of pore and silica (red lines in Figure 5b). The possible biases resulting from that particular choice are discussed in section 4.

Figure 5c shows the final result of the image analysis procedure; for each volume taken in each reconstruction, three functions are obtained for each pore, corresponding to the x' and y' positions of the centerline and to the radius R, as a function of the distance along the pore.

3.3. Pore Position and Shape. The image analysis describes the morphology of each pore with three functions: the two coordinates x' and y' of the center and the radius as a function of the distance z' along the pore. We first proceed to analyze these data in terms of the lattice on which the pores are positioned, and we afterward analyze the shapes of the individual pores. The data presented in the section result from calculations done on a total of about 100 mesopores.

For each height z' in a given reconstruction, the x' and y' positions of the pore centers are fitted to a 2D crystal lattice (see the Supporting Information, SI-3). The base vectors are found to have the same length and to be separated by an angle of 60°, although it was not imposed that the lattice be

---

(49) Crowther, R. A.; de Rosier, D. J.; Klug, A. *Proc. R. Soc. London, Ser. A* **1970**, *317*, 319.

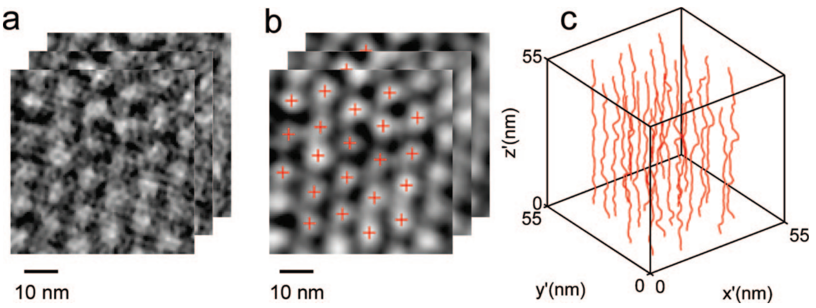

Figure 4. Determination of the height-dependent centers of the pores: (a) each slice orthogonal to z' is taken independently and (b) it is convoluted with a Gaussian kernel of standard deviation 5 pixels; (c) the local maxima (crosses) in the convoluted images are the center of the pores, which is variable in the z' direction.

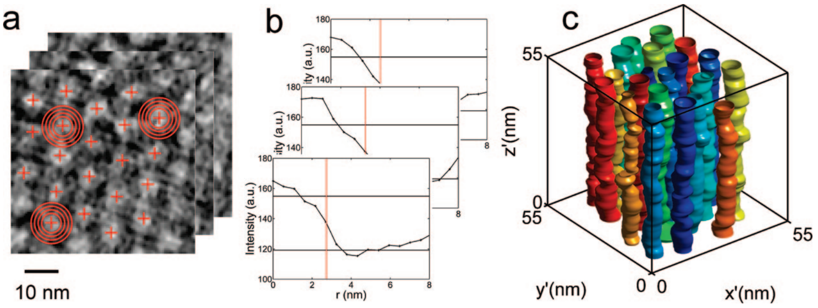

Figure 5. Determination of the z'-dependent radius of the pores: (a) in each slice, the intensity of all pixels at a given distance from the known center is calculated and (b) plotted against the distance. The radius is estimated as the radial distance at which the intensity is exactly intermediate between silica and void (horizontal lines). This provides (c) a description of the tomogram in terms of pores with varying centers and radii.

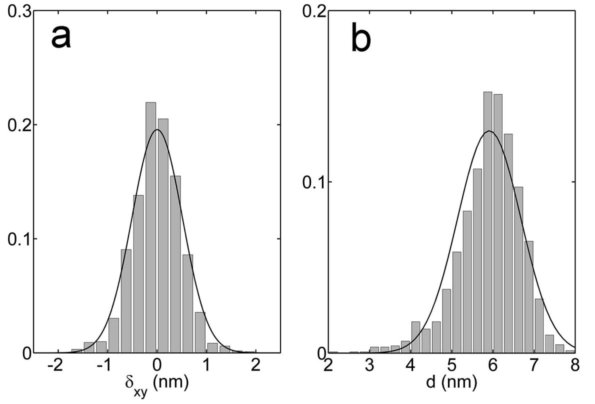

Figure 6. Distributions of (a) the deviation between pore centers and points of the hexagonal lattice δ_{xy} and (b) the local pore diameter d. Both δ_{xy} and d are correlated along a given pore over a distance of 4−5 nm.

hexagonal. The distributions of the deviations between the mesopore centers and the corresponding lattice points are slightly different in the x' and y' directions. Both deviations have a mean of zero, but the standard deviation is about 15% larger in the y' direction. As the x' and y' axes do not correspond to any particular direction of SBA-15, the difference is attributed to the lower resolution in the y' direction,[49] as mentioned in section 3.3.1. In the following, the x' and y' data are pooled and the deviation is referred to as δ_{xy}. Figure 6a is the distribution of δ_{xy}; it has zero mean and standard deviation $\sigma_{xy} = 0.5$ nm. It was also found that δ_{xy} is correlated along any given pore over a distance close to 5 nm (see the Supporting Information, SI-3). This value can be thought of as the length of the zigzags in the pore centerlines.

Figure 6b plots the distribution of the pore diameters. The distribution is slightly skewed toward smaller diameters. It has to be emphasized that the scattering in the pore size results mostly from the variation of size along any given pore, which is responsible for about 70% of the total observed variance. Therefore, the skewness of the distribution points to a few local constrictions of the pores. Most of the distribution is, however, well-described by a Gaussian distribution; the average radius is $R_m = 2.9$ nm and the standard deviation is $\sigma_R = 0.4$ nm. The radius is also correlated along a given pore along distances shorter than about 4 nm (see the Supporting Information, SI-3), which compares to the correlation length of the pore centerlines.

4. Discussion

The morphology of SBA-15 is notoriously complex, as assessed by XRD,[21,50] physisorption,[17,18,34,51] in situ XRD during physisorption,[35,52] as well as from microscopy done on SBA-15 and on negative replicas obtained by infiltration.[24,53−56] The morphological complexity results notably from the corrugation of the main mesopores, from the existence of a complementary porosity connecting them laterally, as well as from microporosity. The present contribution focuses on the quantitative characterization of pore corrugation.

---

(50) Sauer, J.; Marlow, F.; Schüth, F. *Phys. Chem. Chem. Phys.* **2001**, *3*, 5579.

(51) Zukal, A.; Siklova, H.; Cejka, J. *Langmuir* **2008**, *24*, 9837.

(52) Zickler, G. A.; Jähnert, S.; Wagermaeier, W.; Funari, S. S.; Findenegg, G. H.; Paris, O. *Phys. Rev. B* **2006**, *73*, 184109.

(53) Jun, S.; Joo, S. H.; Ryoo, R.; Kruk, M.; Jaroniec, M.; Liu, Z.; Ohsuna, T.; Terasaki, O. *J. Am. Chem. Soc.* **2000**, *122*, 10712.

(54) Choi, M.; Heo, W.; Kleitz, F.; Ryoo, R. *Chem. Commun.* **2003**, *12*, 1340.

(55) Galarneau, A.; Cambon, H.; Di Renzo, F.; Ryoo, R.; Choi, M.; Fajula, F. *New J. Chem.* **2003**, *27*, 73.

(56) Sayari, A.; Yang, Y. *Chem. Mater.* **2005**, *17*, 6108.

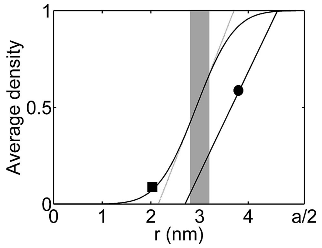

Figure 7. Radial density profiles obtained from XRD using the corona model (•), and from image analysis on the basis of eq 2 (■). The gray zone is the limit between pore sizes obtained from nitrogen adsorption and desorption; *a*/2 is half the distance to the neighboring mesopore.

To analyze the pore corrugation of SBA-15, characterization data are generally analyzed using a linear corona model[21,35,52] with a progressive transition between pore space and either dense or microporous silica. It the case of XRD, the inner and outer radial limits of the corona, r_i and r_o, are obtained from a modeling of the integrated intensities of the scattering peaks. The values of the thickness, $\delta = r_o - r_i$, reported for SBA-15 vary from 1.2−1.3 nm[21,52] to 1.9−2 nm.[21,35] When the thickness obtained from XRD is used in nonlocal density functional model of physisorption, krypton adsorption and desorption isotherms can be predicted very accurately.[34] The values obtained in section 3.1 are $r_i = 2.7$ nm and $r_o = 4.6$ nm, i.e., $\delta = 1.9$ nm; the corresponding density profile is plotted in Figure 7. Despite the suitability of the linear corona for the analysis of bulk characterization data, it is difficult to assess its actual morphological meaning. It may correspond either to an actual microporous corona;[21] it may describe in an average way the corrugation of the pore wall,[22,35] or it may even account for the complementary porosity that connects neighboring mesopores. This issue is addressed in the following, first by comparing the corona to nitrogen adsorption data, and then to image analysis.

In principle, the morphological information obtained from XRD and the fitting of the data with the linear corona, is sufficient to estimate the microporous and mesoporous volumes of SBA-15. Assuming a density of silica of 2.2 g cm^{-3}, the geometrical calculations reported in the Supporting Information (SI-3) enable to analyze the XRD data in terms of the following specific pore volumes: total pore volume $V_{\text{tot}}{}^{\text{XRD}} = 0.33$ cm^3 g^{-1}, of which $V_{\text{center}}{}^{\text{XRD}} = 0.18$ cm^3 g^{-1} is in the center of the pores and $V_{\text{corona}}{}^{\text{XRD}} = 0.16$ cm^3 g^{-1} is in the corona region.

Interestingly, the volumes obtained from XRD are at odds with those derived from nitrogen physisorption in section 3.1: $V_{\text{tot}}{}^{\text{N2}} = 0.66$ cm^3 g^{-1}, $V_{\text{meso}}{}^{\text{N2}} = 0.57$ cm^3 g^{-1}, and microporous volume $V_{\text{micro}}{}^{\text{N2}} = 0.09$ cm^3 g^{-1}. Most strikingly, XRD underestimates the total pore volume by almost a factor 2. This points to the fact that region detected by XRD as being the wall between mesopores is significantly porous, in addition to the corona. An exact matching of the total pore volumes determined by XRD and physisorption requires that the porosity of the wall material be about 30% (see the Supporting Information, SI-3). The same value of 30% has been found on totally different grounds by Hofmann et al.[35] using in situ XRD during krypton adsorption, and similar results have been reported by Galarneau et al. based on adsorption alone.[18] Using the corrected apparent density of the wall, the volumes derived from XRD become $V_{\text{center}}{}^{\text{XRD}} = 0.26$ cm^3 g^{-1}, and $V_{\text{corona}}{}^{\text{XRD}} = 0.23$ cm^3 g^{-1} (see the Supporting Information, SI-3). Two observations are to be done about these values. The first is that the pore volume within the corona is more than twice the microporous volume determined by physisorption (0.09 cm^3 g^{-1}), which suggests that a large fraction of the corona actually fills by multilayer adsorption rather than by micropore filling. The second fact is that the total volume of the pore center and corona is lower than the observed mesopore volume, which shows that multilayer adsorption occurs also in the region of the wall. This is in line with the complementary porosity connecting laterally neighboring mesopores, the existence of which has been repeatedly demonstrated through the characterization of negative replicas of SBA-15, obtained by infiltration.[53−56] The analysis of all samples of ref 21 leads to quantitatively similar conclusions (see the Supporting Information, SI-3). Even more interestingly, it is found that the samples of ref 21 with the largest corona volume $V_{\text{corona}}{}^{\text{XRD}}$ are those that underwent a hydrothermal treatment and that were not microporous according to physisorption. These observations suggest that a mesostructured corrugation of the pores contribute significantly to the corona.

Direct 3D microscopic characterization confirms the existence of pore wall corrugation. The mesopores in the tomograms were described as cylinders with an irregular centerline and a radius that varies along their axes; both effects add up and contribute to the corrugation of the pore walls (Figure 5c). To compare quantitatively the results of microscopy with bulk data, the radial density profile averaged along the pore axis is calculated from the results of image analysis. With a good approximation, the distance x_w from the statistical center of a pore to its wall is the sum of the fluctuations of the center in that particular direction δ_x (or δ_y) and of the radius R. As both δ_{xy} and R are approximately Gaussian-distributed (panels a and b in Figure 6), their sum x_w is also Gaussian-distributed. The probability that x_w be lower than any given value r is therefore calculated as

$$P(x_w < r) = \frac{1}{2}\left[1 + \text{erf}\left(\frac{r - R_m}{\sqrt{2}\sigma_w}\right)\right] \qquad (2)$$

where erf(x) is the error function,[48] and $\sigma_w = \sqrt{\sigma_R{}^2 + \sigma_{xy}{}^2}$. The cumulated distribution $P(x_w < r)$ is equivalent to an average radial density profile; it is plotted in Figure 7. The thickness of the transition region can be estimated approximating eq 2 by a linear ramp (gray line in Figure 7). From the derivative of eq 2 at $r = R_m$, one finds that the thickness δ of the ramp is given by

$$\delta = \sqrt{2\pi(\sigma_R^2 + \sigma_{xy}^2)} \qquad (3)$$

which makes a clear connection between pore corrugation and the linear corona model. Using the values $\sigma_R = 0.4$ nm and $\sigma_{xy} = 0.5$ nm obtained by image analysis, one finds $\delta = 1.6$ nm. The value compares well with the thickness determined from XRD. At this point, it is important to stress the different information carried by Figures 7 and 5b: the thickness of the transition region in Figure 5b originates in the finite resolution of the reconstruction but that in Figure 7 results from the variability of the center and radius along a pore. It is estimated in the Supporting Information, SI-3, that the noise and the finite resolution of the reconstructions could account for at most one-fourth of the estimated amplitude of corrugation δ.

The fact that the entire profile in Figure 7 is shifted toward smaller radii compared to XRD could have two distinct origins. It could be attributed to shrinkage of SBA-15 during the TEM characterization, which has been previously reported for other mesoporous silica.[57] Such a shrinkage is also evident when comparing the lattice size from XRD (10.8 nm) and from microscopy (10.3 nm). Another possible contribution is that the radii may be underestimated by the image analysis. Had the radial intensity profiles (Figure 5b) been cut at a lower intensity to estimate the local radius of the pores, the diameter distribution would have been shifted to larger sizes. This would, however, have had no effect on the breadth of the diameter distribution; the estimated amplitude of the corrugation would have been unchanged.

In addition to the amplitude of the corrugation, which is also available from XRD, the image analysis of electron tomograms provides information on the spatial correlation of the wall corrugation. The correlation length of both the centerlines and radii of the mesopores is found to be about 4−5 nm (Supporting Information, SI-3). This is roughly the length over which the fluctuations in mesopores centers and radii extend along the pore main direction (Figure 5c). The value compares well with the size of the bulges in platinum wires obtained by infiltration of SBA-15.[24] In principle, that morphological information could be available from the analysis of the continuous background of XRD patterns, as also noted by other authors.[35] To the best of our knowledge, however, this has not yet been done.

The characterization done by the present image analysis is not exhaustive. In particular, because of the specific model used for the image analysis, only the main pores of SBA-15 were detected and characterized; the complementary porosity connecting the main pores laterally was not described. The comparison of nitrogen adsorption and XRD showed that the silica wall is about 30% porous, so that the segmented pores shown in Figure 5c account for about 70% of the total porosity of SBA-15. Furthermore, the pore wall corrugation described in this paper, and its agreement with the linear corona model, does not rule out the existence of an atomic scale roughness that is beyond the resolution of the technique. What is clear, however, from the present study is that the nanometer-scaled corrugation of the pore walls is responsible for a large fraction of the roughness of the surface of SBA-15 detected through bulk characterization techniques.

5. Conclusions

Electron tomography and image analysis were successfully applied to characterize the morphology of the mesopores in SBA-15. The latter are modeled in the present approach as irregular cylinders the radius and center of which are variable along their axis. The randomness of the center and of the radius add up and contribute to the corrugation of the surface. The present approach enables to characterize both the amplitude of the corrugation and its spatial correlation along the pores.

The overall amplitude of the corrugation is calculated via the apparent radial density profile of the mesopores, resulting from the irregularity of the wall. The transition region of the average density is found to be 1.6 nm thick, which compares well with the thickness of the linear corona model that can be used to analyze XRD and physisorption data. As for the spatial correlation of the corrugation along the pores, its correlation length is found to be 4−5 nm. The latter value compares with the size of the bulges seen in negative replicas of SBA-15 obtained by infiltration.

The microscopic results of image analysis, together with the macroscopic observation that a large fraction of the corona region actually fills by multilayer adsorption, shows that nanometer-scale corrugation is responsible for a large fraction of the roughness of the surface of SBA-15.

Acknowledgment. C.J.G. acknowledges support from the Fonds de la Recherche Scientifique (FRS-FNRS, Belgium) and from the Subside Fédéral de la Recherche (Université de Liège, Belgium); H.F. and K.P.d.J. from the NRSCC; and M.W. from Johnson Matthey Catalysts.

Supporting Information Available: A movie of an aligned tilt series (SI-1) and a movie through a 3D reconstruction (SI-2) of SBA-15 (MPG). Technical details concerning the methods used in the paper are given in SI-3 (PDF). This material is available free of charge via the Internet at http://pubs.acs.org.

CM803092C

---

(57) Hudson, S.; Tanner, D. A.; Redington, W.; Magner, E.; Hodnett, K.; Nakahara, S. *Phys. Chem. Chem. Phys.* **2006**, *8*, 3467.